Article

Synthetic Mechanism Studies of Iron Selenides: An Emerging Class of Materials for Electrocatalysis

Bo Hou [1,*], David Benito-Alifonso [2], Richard F. Webster [3], David Cherns [4], M. Carmen Galan [2] and David J. Fermín [2,*]

1   School of Physics and Astronomy, Cardiff University, Cardiff CF24 3AA, UK
2   School of Chemistry, University of Bristol, Cantock's Close, Bristol BS8 1TS, UK;
    david.benito@glaia.co.uk (D.B.-A.); M.C.Galan@bristol.ac.uk (M.C.G.)
3   Electron Microscopy Unit, University of New South Wales, Sydney, NSW 2052, Australia;
    r.webster@unsw.edu.au
4   H H Wills Physics Laboratory, University of Bristol, Tyndall Avenue, Bristol BS8 1TL, UK;
    D.Cherns@bristol.ac.uk
*   Correspondence: houb6@cardiff.ac.uk (B.H.); David.Fermin@bristol.ac.uk (D.J.F.)

Abstract: Solution-processed iron selenide nanocrystals (NCs) have recently attracted considerable attention in electrocatalysis water splitting. Nevertheless, a primary challenge in current iron-based NCs chemical synthesis is controlling phase purities between each chalcogen (monochalcogenide, dichalcogenides, and oxides), which requires a comprehensive understanding of the reaction mechanisms at the early stages of nucleation. Herein, we investigate the fundamental steps in transforming molecular organoiron and organoselenium precursors to iron selenides NCs with the view of developing universal synthesis protocols for phase pure metal selenium and metal oxides NCs. The main intermediate species and volatile by-products are identified by high-resolution electron microscopy and Nuclear Magnetic Resonance (NMR) spectroscopy (^{1}H, ^{13}C, and ^{31}P). Experimental evidence suggests that the phase determining factor is the coordinating reactivity difference between olefins (1-octadecene, oleylamine), tributylphosphine and trioctylphosphine associated with their corresponding Se bond cleavage. This work proposes organoselenium interconversion reaction mechanisms during iron selenides synthesis, offering a universal synthetic strategy for other electrocatalytically or photocatalytically active layered metal selenides materials.

Keywords: iron dichalcogenide; iron selenides; iron oxide; synthetic mechanisms; electrocatalysis

1. Introduction

Since the discovery of superconductivity from iron compounds [1,2], iron-based semiconductors, particularly iron selenides, have attracted great interests from physicists and chemists [3–10]. Considerable research on iron selenides has been carried out not only to aim at high-temperature superconductivity but also various other novel applications [4,11]. For instance, among the complex phase diagram, FeSe and FeSe$_2$ have been demonstrated as photo-absorbers for photovoltaics [12], anode materials for sodium-ion batteries [8,10], cathode materials for lithium-air batteries [5], and non-linear optical materials for bioimaging [9,13]. Recently, excellent electrocatalysis performance in oxygen evolution reaction (OER) [6,14], hydrogen evolution reaction (HER) [15–17], and overall water splitting [7,11] have also been discovered and demonstrated in FeSe$_2$ and FeSe. Indeed, iron selenides present strong potential and unique electrical and optical properties for electrocatalysis, and their performance is strongly related to the stoichiometric ratio between Fe and Se and their phase purity [6,8,11,16–18].

Iron selenides could crystallize in the form of FeSe (α-FeSe and β-FeSe), Fe$_3$Se$_4$, Fe$_7$Se$_8$ and FeSe$_2$, depending on the composition of the binary phase. The phase diagram of iron selenides is similar to the NiAs system [19]. The structure of iron selenides may be

hexagonal, NiAs-like structures [20] with a composition of Fe_7Se_8 (H-phase) or as a monoclinic structure of the same phase with composition Fe_3Se_4 (M-phase). FeSe crystallizes in tetragonal (PDF = 85-0735) or hexagonal structure (PDF = 75-0608), while $FeSe_2$ crystallizes in cubic (PDF = 48-1881) or orthorhombic marcasite-type structures (PDF = 21-0432) [21]. Regarding the bandgap of FeSe, large discrepancies can be found in the literature ranging from 0.14 eV to 3.00 eV [22–24]. $FeSe_2$ has been reported as a p-type material with a bandgap of around 1 eV [25].

FeSe and $FeSe_2$ have been fabricated using several high-temperature approaches such as metal-organic chemical vapor deposition [26], mechano-synthesis [27], vapor selenization [21,25,28,29], mechanical alloying [3,30,31], reactive sputtering, and spray pyrolysis [32–34]. However, the products were extremely unstable at high temperature, giving rise to phase changes in the deposited film [18]. Therefore, synthetic routes at low temperatures have been developed, including chemical bath deposition [24], electrodeposition [35], and organic metallic chemical synthesis [36–39]. Conventional 'hot-injection' method is commonly adopted in synthesizing metal chalcogenide NCs [40–42] such as CdSe [43–50], ZnSe [51–54] CuInZn(SSe)$_3$ [55–57], CuZnSn(SSe)$_4$ [58,59], PbS [55,60–63], PbSe [64–66], HgSe [67,68] or HgTe [69,70]. Until now, organic metallic reactions via 'hot-injection' and corresponding thermolysis approaches attracted the most interest for synthesizing iron selenides due to their better phase and crystal structural controllability than the other low-temperature synthesis methods [9,13,71–74]; however, a detailed understanding of its chemical reaction mechanisms was rarely reported.

In the present work, we investigate the fundamental steps in transforming molecular organoiron and organoselenium precursors to iron selenides NCs during the organometallic reaction to develop universal synthetic protocols for preparing phase pure FeSe and $FeSe_2$ NCs. Four common organic reaction media have been chosen, and the main intermediate species and volatile by-products were identified by Transmission Electron Microscopy (TEM), High Resolution Transmission Electron Microscopy (HRTEM) and NMR spectroscopy (^{1}H, ^{13}C, and ^{31}P). Phosphine Lewis bases such as tributylphosphine (TBP) or trioctylphosphine (TOP) were chosen due to their strong coordination to the chalcogenide component. In addition, long alkane chain olefin compounds such as 1-octadecene (1-ODE) and oleylamine (OLA) were also selected since both reagents are the most popular phosphine-free solvents for metal chalcogenide nanocrystal synthesis. Experimental evidence suggests that the phase determining factor is the coordinating reactivity difference between olefins (1-ODE and OLA), TBP, and TOP associated with their selective Fe-Se bond cleavage.

2. Results and Discussion

2.1. Chemical Reaction Mechanisms in the 'Hot-Injection' Approach

A double cold trap apparatus was employed to extract the volatile reaction intermediates. Se precursor was prepared by dissolving Se in TBP. The iron precursor was formed by iron (II) acetate (Fe(AC)$_2$) reacting with stearic acid (SA) in 1-ODE. As shown in Figure S1 (Supplementary Information), the reaction product generated from the first reaction of iron acetate with SA and 1-ODE is monitored. The volatiles generated from the reaction were trapped in the double 'cold trap', which was equipped with a Dewar with liquid nitrogen. The formation of the iron precursor was examined by taking aliquots during the heating stage prior to the injection of Se precursors.

Figure 1a,b shows ^{1}H and ^{13}C NMR analysis of the product (Sample I) collected by the 'double trap', which was generated after loading iron acetate, SA and 1-ODE into the reaction vessel and heating at 60 °C and 130 °C for half an hour, respectively. In Figure 1a, the formation of acetic acid is revealed by the strong intermolecular hydrogen bonding in carboxylic acid dimers, which leads to very low-field broad signal δ = 9.74 (sample I) and 11.00 (commercial, acetic acid, ≥99.7%, Sigma-Aldrich) in the range of 9–15 ppm. The up-field proton signal is similar between Sample I and commercial acetic acid, such as the singlet at around 2 ppm is also characteristic (CH$_3$) of acetic acid. Further evidence is

provided by the ^{13}C NMR spectra, as shown in Figure 1b, in which identical carbon shifts are observed for Sample I and acetic acid standard sample.
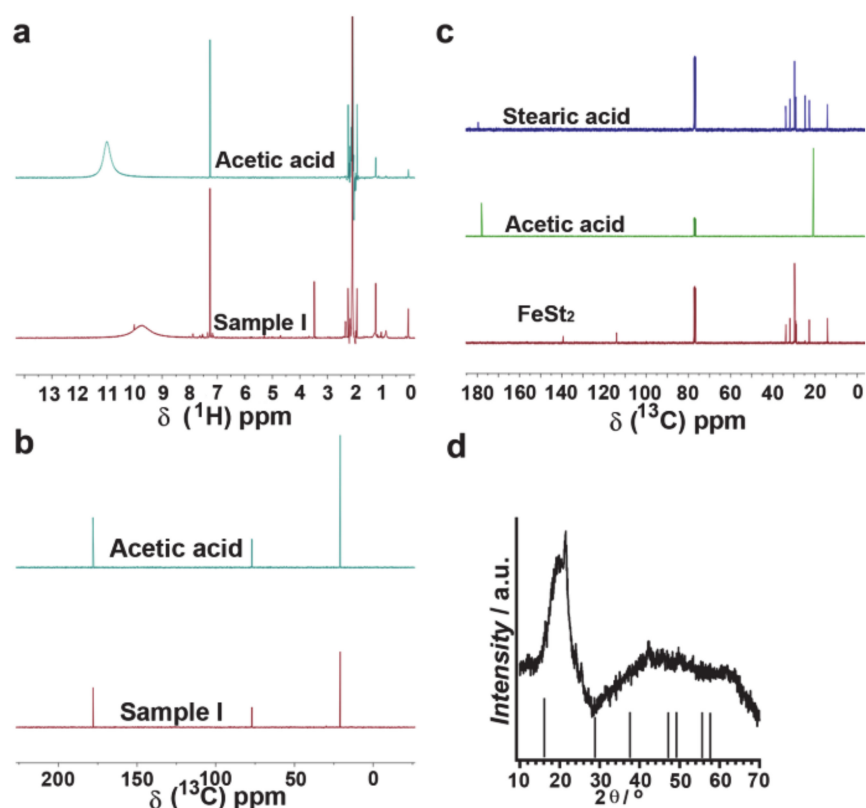

Figure 1. ^{1}H (**a**) and ^{13}C NMR (**b**) analysis of volatile species Sample I collected from 'cold trap'. ^{13}C NMR analysis of the reaction intermediate, which was taken during Fe(Ac)$_2$, reacted with SA in the presence of 1-ODE (**c**). X-ray Powder Diffraction (XRD) diagram of final product generated through hot injection of TBP-Se into iron precursor prepared by Fe(AC)$_2$ reacted with SA in the present of 1-ODE (**d**).

Figure 1c shows the ^{13}C NMR analysis of iron-containing species collected from the iron precursor. Compared to the ^{13}C NMR spectra of standard SA (analytical grade, Fisher Scientific) and acetic acid, the reaction solution shows negligible acetic acid content. On the other hand, iron stearate (FeSt$_2$) can be resolved with identical chemical shifts to stearic acid except for the absence of carbonyl's chemical shift (^{13}C, $\delta = 180$ ppm) ascribed to the screening effect upon bonding with iron.

However, after injection of Se precursor (Se in TBP), no color change occurs even when the heating time is extended to 30 min. Furthermore, as shown in Figure 1d, there are no characteristic or prominent lattice reflections from the XRD analysis of the crude solution, especially at large angles. From the result achieved so far, the only conclusion is the formation of amorphous metal or organic iron complex rather than highly crystalline nanoparticles.

Based on the NMR and XRD analysis, a plausible reaction pathway is proposed in Scheme 1. Fe(AC)$_2$ reacts with SA in the presence of 1-ODE via a ligand exchange reaction, generating FeSt$_2$ as iron precursors and volatile acetic acid. Due to the strong bonding between Se and phosphorus, the Se-TBP bond is not readily cleaved under these conditions after the injection of Se precursors. Consequently, no crystalline products are formed in the end.
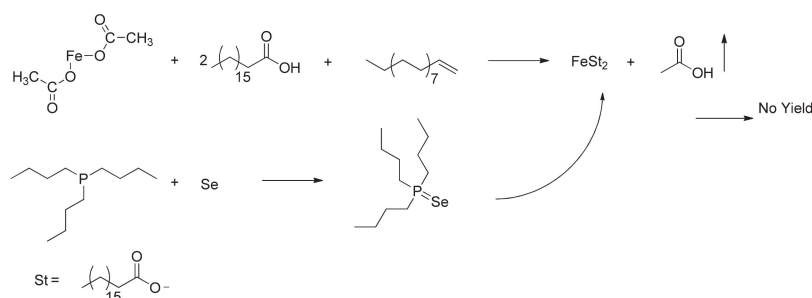
Scheme 1. Plausible reaction pathway of the synthesis of FeSe$_2$ by 'hot-injection' method employing Fe(AC)$_2$ and SA as an iron precursor, and TBP for solubilization of Se.

The second investigation is carried out by adjusting Se precursors' reactivity from replacing TBP by OLA. Since the coordination between OLA and Se is weaker than that of phosphines [45,55], we anticipate a more labile Se-OLA bond cleavage, thus accelerating the reaction of Se with FeSt$_2$ and resulting in the formation of the desired iron selenide NCs.

Figure 2a shows the XRD of as-prepared nanocrystals obtained in the presence of OLA. In contrast to the TBP approach, highly crystalline orthorhombic FeSe$_2$ is achieved, with each XRD feature assigned according to the standard PDF card index (PDF = 21-0432 and 74-0247).
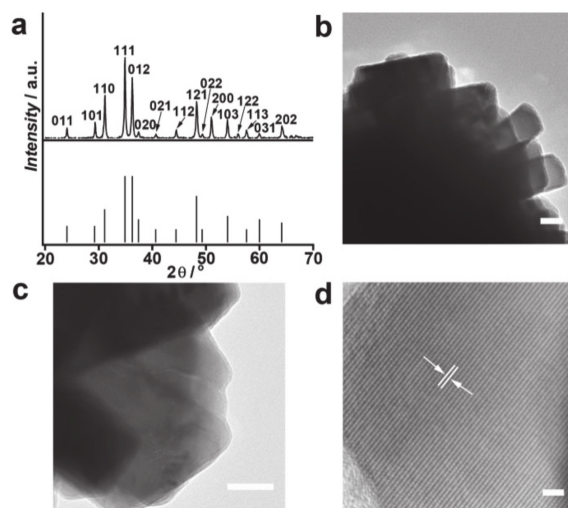

Figure 2. (**a**) Powder XRD pattern of as-prepared FeSe$_2$ nanocrystals through employing FeSt$_2$ as an iron precursor and OLA for solubilization of Se. The vertical lines on the bottom correspond to orthorhombic marcasite-type structures of FeSe$_2$ (PDF = 21-0432 and 74-0247). (**b,c**) TEM analysis of as-prepared FeSe$_2$, the scale bar is 50 nm. (**d**) HRTEM analysis of as-prepared FeSe$_2$ resolved the reflection from the (110) plane, with a lattice spacing of 3.8 ± 0.2 Å, the scale bar is 2 nm.

Figure 2b,c displayed the TEM analysis results, which exhibits the expected layer type morphology] The HRTEM in Figure 2d resolved the reflection from the (110) plane, with a lattice spacing of 3.8 ± 0.2 Å, which is close to the value for single crystal orthorhombic iron diselenide.

Based on the XRD, TEM and HRTEM analysis results, a plausible reaction pathway of the second approach is proposed, as shown in Scheme 2. The mechanism for the FeSt$_2$ formation is the same as Scheme 1. However, the reaction between selenium and OLA will generate organoselenium complexes, as reported in our previous works [45,59] These less reactive organoselenium complexes react with FeSt$_2$ at elevated temperature and facilitate the formation of FeSe$_2$ NCs.
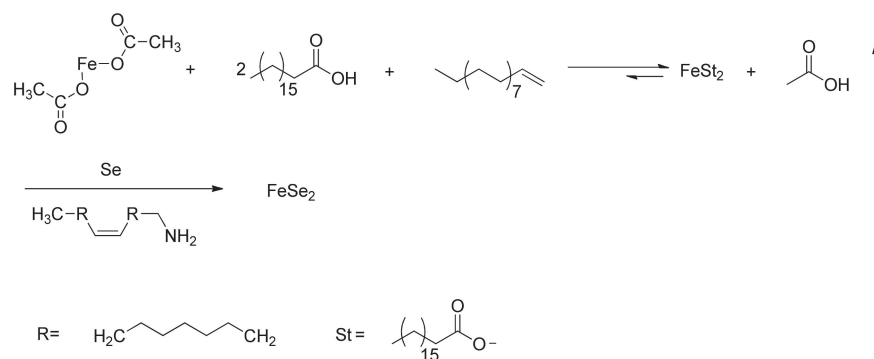
Scheme 2. Plausible reaction pathway for the second approach for the synthesis of $FeSe_2$, employing $FeSt_2$ as an iron precursor and OLA for solubilization of Se.

The third investigation involves the replacement of 1-ODE by OLA in the iron precursor. In that case, both iron and Se precursor were prepared in the presence of OLA. After injection of the Se precursor, strongly magnetic particles are formed, as revealed by the strong adsorbing on the magnetic stirring bars. TEM analysis revealed spherical shape nanoparticles. Figure 3b shows the XRD analysis of the final product from the third approach, with no evidence of iron selenides. High purity Fe_3O_4 nanocrystals are found as confirmed by the well-aligned XRD reflections compared with standard face-centered cubic Fe_3O_4 PDF card (PDF = 75-0033). The crystal domain size is calculated to be 10.9 ± 4.3 nm from the Scherrer equation. HRTEM analysis resolved the reflection from the (220) plane in Figure 3c with a lattice spacing of 3.0 ± 0.2 Å confirmed the cubic structure. Furthermore, the (111) plane (Figure 3d) with a lattice spacing of 5.0 ± 0.2 Å also resolved, which are close to the bulk Fe_3O_4 structure value.
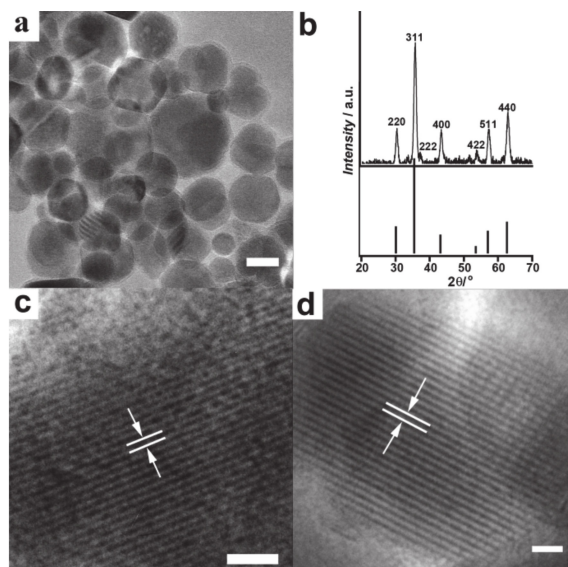
Figure 3. TEM (**a**), XRD (**b**) and HRTEM (**c**,**d**) analysis of as-prepared Fe_3O_4 nanoparticles. (**a**) TEM analysis of Fe_3O_4 nanoparticles with scale bar equal to 20 nm. (**b**) Powder XRD pattern of as-prepared Fe_3O_4 NCs by Scheme 3, the vertical line on the bottom corresponds to face centered cubic Fe_3O_4 (PDF = 75-0033). (**c**,**d**) HRTEM of Fe_3O_4 resolving the lattice spacing of the (220) plane is 3.0 ± 0.2 Å and (111) plane is 5.0 ± 0.2 Å. The scale bar in HRTEM images is all equal to 2 nm.
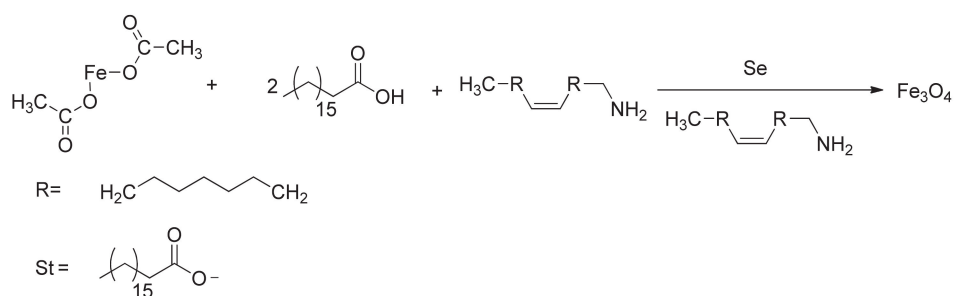
Scheme 3. Plausible reaction scheme for the synthesis of Fe_3O_4 from $Fe(Ac)_2$ and OLA. It should be noted that OLA shows on the arrow refer to the solvent for preparing the Se precursor.

Based on XRD, TEM, and HRTEM analysis of the data, a plausible reaction pathway for the third approach is proposed in Scheme 3. The critical step in iron precursor formation is the anion exchange process driven by the depletion of acetic acid and the construction of $FeSt_2$. As shown in Scheme 3, when 1-ODE is replaced by OLA, the formation of $FeSt_2$ is prohibited by a condensation reaction between OLA and SA instead of the anion exchange reaction between SA and acetic acid. Therefore, when elevating the temperature after the injection of Se precursors, iron acetate will first undergo a thermolysis reaction generating Fe_3O_4 NCs rather than reacting with Se species.

Furthermore, as discussed earlier in Schemes 2 and 3, the formation of $FeSt_2$ and Se-C organoselenium species is crucial to achieving high purity $FeSe_2$ without the formation of Fe_3O_4. Therefore, an excess amount of SA, vacuum drying and suitable selenium precursors are the critical factors in the $FeSe_2$ NCs synthesis through the 'hot-injection' approach. It should be noted that the organic metallic chemical synthesis of iron nanoparticles, iron metal or iron-nonmetal alloy is also a rather complex reaction process [59]; however, similar approaches to our current work could be carried out in the future to elucidate the underlying synthetic mechanisms.

2.2. Selenium Extraction for the Synthesis of FeSe Nanoparticles

The synthesis of FeSe was carried out through the extraction of selenium from $FeSe_2$ by TBP, analogous to the previous report [74]. However, no FeSe nanocrystals could be found in the final solution after the chemical extraction process (Figure S2). The XRD analysis in Figure S2 of the crude solution shows no prominent reflections from FeSe NCs, especially at large angles. A plausible chemical pathway can be proposed, as shown in Scheme S1. It can be concluded that after reacting with TBP, all the $FeSe_2$ changed to amorphous metal or organic iron complex rather than highly crystalline NCs.

An alternative approach was carried out by replacing TBP with TOP. During the reaction between $FeSe_2$ and TOP, 1 mL of the reaction solution was syringed out under Ar protection, and J. Young NMR tube was employed for ^{31}P NMR analysis (denoted as Sample II) since TOP is air sensitive. Aliquots were also taken out for monitoring crystal structure evolution by XRD analysis. Figure 4 shows the typical ^{31}P NMR analysis result. Taking TOP standard as a reference, a new singlet with a chemical shift of $\delta = 36.28$ ppm is appeared after the phase transformation. The signal is indexed to P = Se correlation which is consistent with the literature value [75].

The as-prepared FeSe nanoparticles show flake-like features, as shown in Figure 5a of the TEM analysis. The HRTEM image in Figure 5b resolves the lattice fringes of the (001) plane, with a lattice spacing of 5.9 ± 0.2 Å, consistent with the bulk FeSe tetragonal crystal value (PDF = 85-0735). Figure 5c shows the XRD analysis of the aliquots during the extraction reaction. Well-defined reflections can be revealed in Figure 5c, which displays series of reflection evolutions during phase transformation from orthorhombic $FeSe_2$ to a tetragonal FeSe crystal structure.
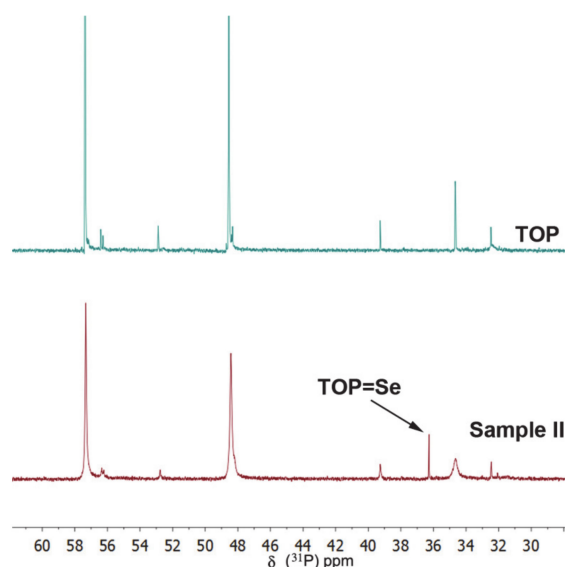
Figure 4. ^{31}P NMR analysis of reaction intermediates during the reaction of FeSe$_2$ with TOP. The top spectrum corresponds to standard TOP. The bottom spectrum corresponds to Sample II, taken from the crude reaction mixture by J. Young NMR tube.
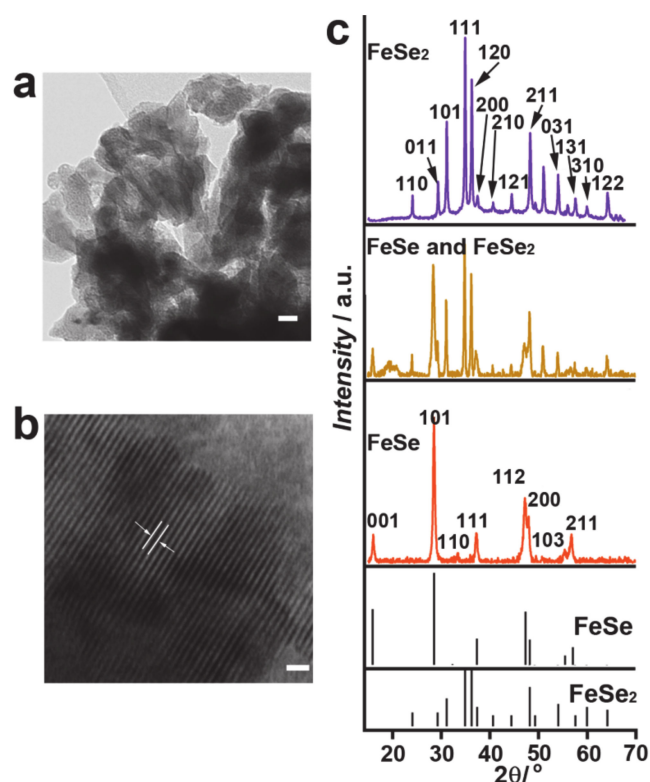
Figure 5. TEM (**a**) and HRTEM (**b**) analysis of as-prepared FeSe NCs, the lattice spacing is 5.9 ± 0.2 Å, and the scale bar is 20 nm and 2 nm, respectively. (**c**) A series of XRD patterns derived from preparing FeSe nanocrystals through extracting Se from FeSe$_2$. The vertical line on the bottom corresponds to tetragonal FeSe (PDF = 85-0735) and orthorhombic marcasite-type structures of FeSe$_2$ (PDF = 21-0432), respectively.

Based on the analysis of reaction intermediates extracted from TEM and XRD, a plausible reaction mechanism was proposed, as shown in Scheme 4. FeSe$_2$ reacted with TOP and diffuse half the equivalents of Se generating FeSe and TOPSe. It should be noted

that the delicate detail step reaction mechanism remains unclear; however, a conclusive claim can be made that the amount of TOP added into the solution and the reaction duration are crucial factors. For instance, we found an excess amount of TOP or extending the reaction time will result in the formation of amorphous materials instead of FeSe NCs.
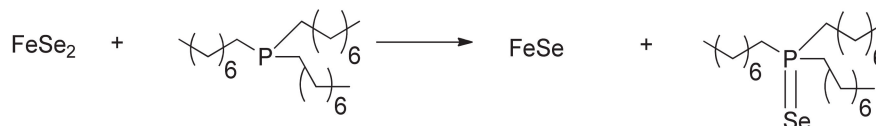
Scheme 4. Plausible reaction scheme for the synthesis of FeSe from $FeSe_2$ and TOP.

2.3. Optical Properties Analysis

Reflectance is the fraction of light reflected from a surface as a function of wavelength. When properly measured, reflectance provides information about the optical properties of materials, since the light that is not reflected is either absorbed due to its chemical composition, or is scattered and/or transmitted, depending on mechanical structure.

Generally, the surfaces of substances reflect light differently depending on their texture. Smooth surfaces such as mirrors reflect the beam in exactly the same direction as the incident beam. On the other hand, rough surfaces substance exhibit diffuse reflection, whereby the rays of the incident beam are scattered in all directions. Normally, a typical surface is in neither smooth or completely rough, and therefore has both specular and diffuse components. Therefore, using an integrating sphere which collects all of the beams reflected by the material surface, one can estimate the optical properties of the substance. To extract the band gap from reflectance measurements, the functions proposed by Tau [76] and Kubelka-Munk were employed (see derivative process below).

$$h\nu\alpha^{(1/n)} = A\left(h\nu - E_{gap}\right) \tag{1}$$

$$F(R_\infty) = \frac{(1 - R_\infty)^2}{2R_\infty} = \frac{k}{s} = \frac{Ac}{s} \tag{2}$$

$$(h\nu * F(R_\infty))^2 = A\left(h\nu - E_{gap}\right) \tag{3}$$

where: h: Plank's constant, ν: frequency of vibration, α: absorption coefficient, E_{gap}: band gap, A: proportional constant. The value of n is denoted according to the nature of the materials: for direct allowed transition, $n = \frac{1}{2}$; for direct forbidden transition, $n = 3/2$; for indirect allowed transition, $n = 2$; for indirect forbidden transition, $n = 3$. For both FeSe and $FeSe_2$, direct allowed transitions have previously been reported. Therefore, in this case, the value of n in Equation (1) is 2.

Figure 6a,e shows the multiple total reflection measurements on different areas of the glass slides covered by $FeSe_2$ and FeSe, respectively. Since it is difficult to ensure the homogeneous coverage of the slides by drop-casting, the position of the slide was directed toward the light source together with multiple measurements to minimize errors. By transforming the reflectance experimental data (Figure 6a,e) following Equations (1)–(3), the optical band gap of $FeSe_2$ (Figure 6b–d) and FeSe (Figure 6f–h) were predicted from the intercepts of the tangent line of the curves to the abscissa.

High absorption and low reflectance can be observed from Figure 6a, indicating that the bandgap of $FeSe_2$ is less than 1.2 eV. Based on the Tau and Kubelka-Munk equations, [76] the optical band gap of $FeSe_2$ is estimated to be 0.67 eV. For FeSe NCs, the reflectance measurement shows a change in the reflectance at a wavelength of around 700 nm for all three measurements. By performing the same transformation, the optical band gap of FeSe is estimated to be 1.73 eV.
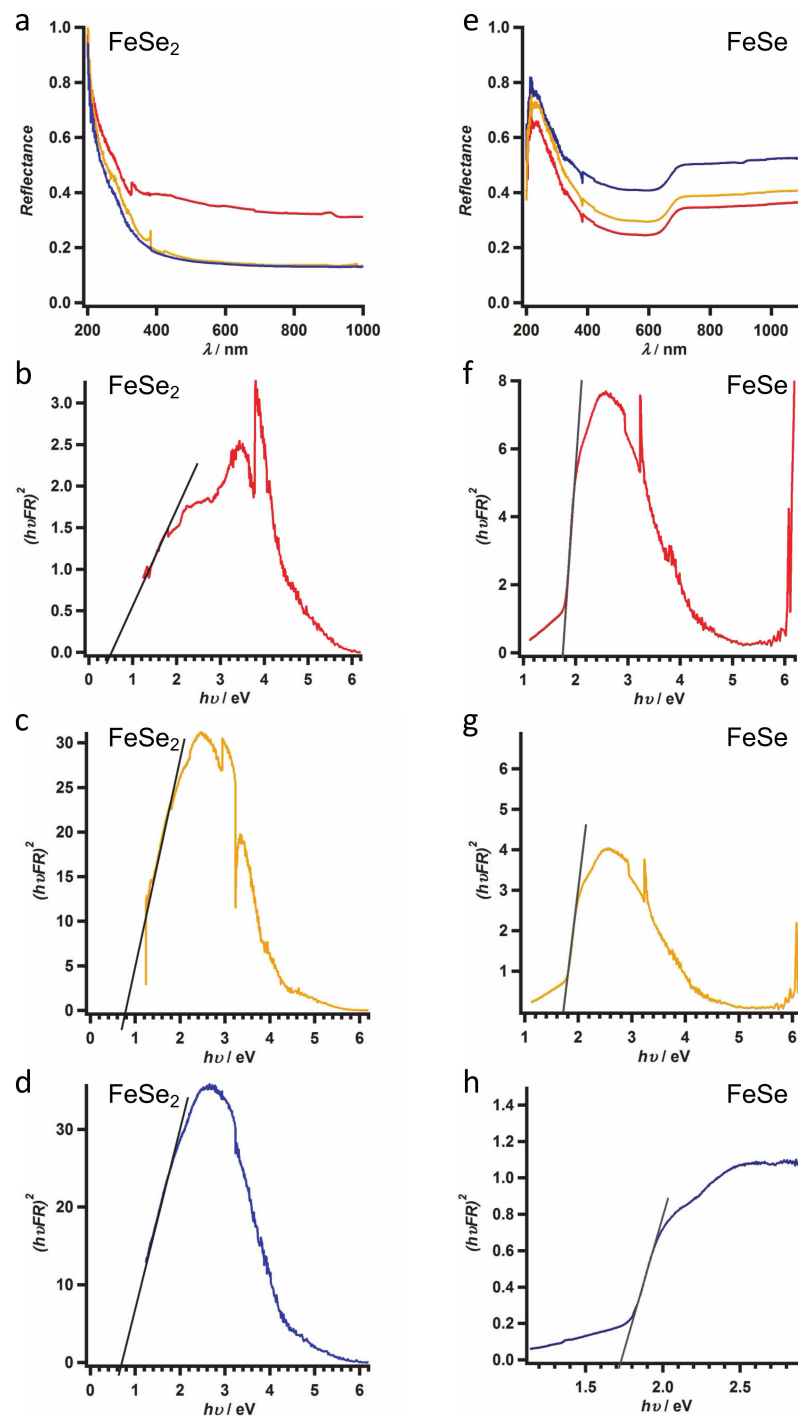
Figure 6. Optical band gap estimation of FeSe$_2$ (**a**–**d**) and FeSe (**e**–**h**) from the reflectance measurement, different colour solid line attributed to the same sample in different measurement. The bandgap values of FeSe$_2$ (**b**–**d**) and FeSe (**f**–**h**) are collected from the intercepts on the abscissa.

It should be noted that in Figure 6a,e, the reflectance increases swiftly when the incident light has a wavelength below 400 nm. This could be attributed to a scattering effect. In the Rayleigh approximation as depicted in Equation (4):

$$I = I_0 \left(\frac{1 + \cos^2 \theta}{2R^2} \right) \left(\frac{2\pi}{\lambda} \right)^4 \left(\frac{n^2 - 1}{n^2 + 2} \right)^2 \left(\frac{d}{2} \right)^6 \tag{4}$$

where I_0 is the light intensity before the interaction with the particle, R is the distance between the particle and the observer, θ is the scattering angle, n is the refractive index of the particle, and d is the diameter of the particle. For instance, taking some common semiconductors as examples, and setting the distance between the particle and observer at 0.2 m, the size of the particle as 100 nm, I_0 equal to unity, and taking and the refractive index of CdSe, [77] CdTe, [77] CdS, [77] ZnSe, [77] ZnO, [78] TiO_2, [79] PbSe [77] from literature values. The evolution of I as a function of λ and refractive index n is shown in Figure 7. From the plot, an increase in scattering is observed as the wavelength of incident light decreases. Further explanation should be given about the index of refraction, since the index of refraction of materials is also a function of wavelength. The values taken from the literature are measured under different wavelength conditions. However, in the current study, it is assumed that the refraction index of the selected materials remains constant during the light scattering process, and focusing only on the variation of light scattering at the surface of the semiconductor as a function of incident light wavelength. The term scattering refers to a general physical process, such as when the ray form of light, sound or even moving particles are forced to change their trajectory by one or more localized non-uniformities in the medium which they are in. Reflection can be simply understood as being a special type of scattering process, whereby, the line normal to the surface equally divides the angle between incident light and reflected light, in accordance with the so-called law of reflection. Therefore, as noted before, a light scattering will induce the enhancement of reflection within the integrating sphere reflection measurement.
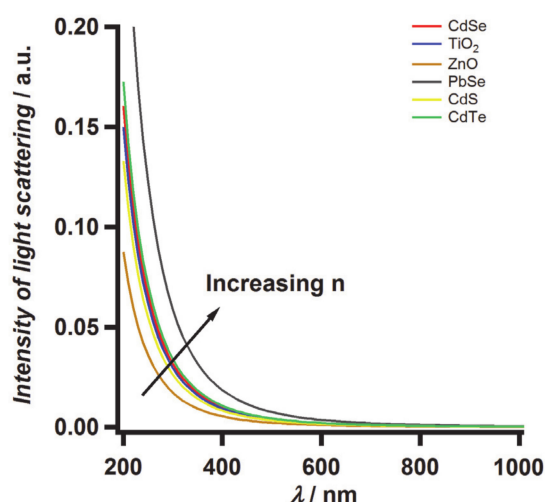

Figure 7. Rayleigh scattering of semiconductors as a function of wavelength, as determined by employing Equation (4). The arrow indicates the effect of increasing of refractive index.

3. Materials and Methods

3.1. 'Hot-Injection' Approach

The synthesis of $FeSe_2$ was carried out under standard oxygen/water-free conditions using a Schlenk line. Two types of selenium precursors are prepared: selenium in oleylamine (OLA) and selenium in tributylphosphine (TBP). Se in oleylamine: 0.1342 g (1.7 mmol) Se (99.99%, Sigma-Aldrich, Dorset, UK) and 10 mL oleylamine (technical grade, 70%, Sigma-Aldrich, Dorset, UK) were loaded into a two-neck flask under Ar and vacuum drying at 60 °C and 130 °C for 30 min, respectively. Then, Se was allowed to dissolve completely by heating at 200 °C under Ar overnight. Se in TBP: a Se stock solution (1 M) was prepared by dissolving 0.79 g of selenium in 10 mL of TBP, yielding a colorless solution.

Two types of iron precursors were prepared, which are $Fe(AC)_2$ in 1-octadecene (1-ODE) and $Fe(AC)_2$ in OLA. In 1-ODE: 0.34786 g (2 mmol) $Fe(Ac)_2$ (95%, Sigma-Aldrich, Dorset, UK), 1.4224 g (5 mmol) stearic acid (SA, analytical grade, Fisher Scientific, Lough-

borough, UK), and 5.0 mL 1-ODE (technical grade, 90%, Sigma-Aldrich, Dorset, UK) were loaded into a 50 mL two neck flask under Ar. After loading, the whole system is vacuum dry at 60 °C and 130 °C for half an hour, respectively. In OLA: a similar precursor solution was prepared but replacing 1-ODE with OLA.

The Se precursor (transparent colorless for Se in TBP or transparent yellowish solution for Se in OLA) was injected into the iron precursor (prepared in 1-ODE or OLA) under Ar at 130 °C.

After injection, the temperature increased to 200 °C under vigorous stirring. The reaction temperature was held at 200 °C for 20 min before cooling to room temperature. Toluene (7 mL) was injected into the final solution, and the solution stored under Ar. The purification of as-prepared $FeSe_2$ involves precipitation by adding isopropyl alcohol and centrifugation at 8000 rpm for 10 min. To remove the excess of organic stabilizer, centrifugation was carried out three times.

3.2. TBP and TOP Extraction Se from Iron Diselenide

The procedure is similar to the method reported recently8] Approximate 30 mg of purified $FeSe_2$ was loaded into a two-neck flask under Ar. 10 mL TOP or TBP was added, and the mixture was dried in a vacuum at 60 °C for 30 min. The temperature increased to 180 °C and held at this temperature for 50 min with vigorous stirring. The mixture was allowed to be cooling down to room temperature. The NCs were purified by precipitation with hexane and methanol mixture and centrifugation (3 times). The final purified FeSe NCs were re-dispersed in toluene and stored under Ar.

3.3. NMR, XRD and TEM Methodologies and Instrumentation

Reactions requiring anhydrous conditions were performed under an atmosphere of either anhydrous nitrogen or argon. All glassware was flame-dried prior to use, and glass syringes and needles were placed in an oven (150 °C) for at least 2 h and allowed to cool in desiccators under an atmosphere of anhydrous nitrogen. 1H NMR and ^{13}C NMR spectra were measured in a 400 MHz Varian INOVA 400 instrument (Varian, Crawley, UK). Chemical shifts are quoted in parts per million (ppm) and referenced to $SiMe_4$ (1H NMR 0 ppm) and $CDCl_3$ (^{13}C NMR 77.16 ppm). The ^{13}C NMR sequence parameters were set up as follows: 45° pulse of 7.70 µs, τ = 1.0 s, and acquisition time of 1.28 s. The ^{31}P NMR spectra were measured in a Jeol ECP (Eclipse) 300 instrument (JEOL, Herts, UK). The crystal structure of the products was investigated by powder XRD (BRUKER D8, Cu Kα radiation λ = 1.54 Å, Durham, UK), JEOL 2011 200 kV Hi Resolution TEM (HRTEM, JEOL, Herts, UK) fitted with an EDX Oxford Instruments ISIS 300 system (Oxford Instruments plc, Abingdon, UK).

3.4. Optical Properties Analysis

Typically, $FeSe_2$ or FeSe nanocrystals which dispersed in toluene were drop-casting onto a quartz slide. Then, the reflectance of the slides is analyzed at a 90-degree incident bean angle position on a Perkin Elmer Lambda 35 spectrometer (PerkinElmer, Beaconsfield, UK).

4. Conclusions

In summary, $FeSe_2$, FeSe and Fe_3O_4 NCs were successfully produced through a well-controlled synthetic strategy. The underlying reaction mechanism was, for the first time, monitored by in situ NMR analysis of intermediates generated during the synthesis of $FeSe_2$ from $Fe(AC)_2$. Plausible reaction mechanisms are proposed based on the detected intermediate species. Upon understanding the chemical reaction process, iron oxide NCs were synthesized by thermolysis reaction. It was found that Fe_3O_4 is the most stable iron oxide phase during the thermolysis of iron acetate, rather than Fe_2O_3 or FeO. By 'chemical etching' of $FeSe_2$, tetragonal crystal structure FeSe nanoparticles were synthesized successfully. As determined by ^{31}P NMR, TOP was found to play a role in the lattice

diffusion of Se from FeSe$_2$. The formation of FeSe was found subsequently with the cleavage of the Fe-Se bond and the formation of the Se-P bond. A plausible reaction mechanism of this phase transformation process was also proposed. The optical properties of as-prepared FeSe and FeSe$_2$ were investigated by integrating sphere total reflection measurements. It was found that the optical band gap of FeSe$_2$ is around 0.67 eV, and FeSe is 1.73 eV. Given the complex nature of the phase diagram of iron chalcogenides, the fundamental understanding of phase pure synthesis of FeSe and FeSe$_2$ NCs are of paramount importance for their photocatalysis and electrocatalysis applications. This work provides comprehensive studies on the organoselenium interconversion reaction mechanisms during iron selenides synthesis, which offer a universal chemical synthetic pathway for preparing phase pure electrocatalytically or photocatalytically active layered metal selenides materials.

Supplementary Materials: The following are available online at https://www.mdpi.com/article/10.3390/catal11060681/s1, Figure S1: A 'double cold trap' set up for the collection of the volatile reaction intermediate species, Scheme S1: Plausible reaction mechanism for the synthesis of FeSe from FeSe$_2$ and TBP, Figure S2: The powder XRD pattern of the final product generating from the preparation of FeSe, which employs TBP as an extraction reagent.

Author Contributions: Conceptualization, B.H. and D.J.F.; methodology, B.H., D.B.-A., R.F.W.; validation, D.C., M.C.G. and D.J.F.; formal analysis, B.H., D.B.-A., R.F.W.; investigation, B.H., D.B.-A., R.F.W.; resources, D.C., M.C.G. and D.J.F.; data curation, D.C., M.C.G. and D.J.F.; writing—original draft preparation, B.H. and D.J.F.; writing—review and editing, D.B.-A., R.F.W., D.C. and M.C.G.; visualization, B.H., D.B.-A., R.F.W.; supervision, D.C., M.C.G. and D.J.F.; project administration, D.J.F.; funding acquisition, M.C.G., and D.J.F. All authors have read and agreed to the published version of the manuscript.

Conflicts of Interest: The authors declare no conflict of interest.

References

1. Kamihara, Y.; Watanabe, T.; Hirano, M.; Hosono, H. Iron-Based Layered Superconductor La[O$_{1-x}$F$_x$]FeAs (x = 0.05−0.12) with T$_c$ = 26 K. *J. Am. Chem. Soc.* **2008**, *130*, 3296–3297. [CrossRef] [PubMed]
2. Yi, W.; Sun, L.; Ren, Z.; Lu, W.; Dong, X.; Zhang, H.-j.; Dai, X.; Fang, Z.; Li, Z.; Che, G.; et al. Pressure effect on superconductivity of iron-based arsenic-oxide ReFeAsO$_{0.85}$ (Re = Sm and Nd). *EPL Europhys. Lett.* **2008**, *83*, 57002. [CrossRef]
3. Hsu, F.-C.; Luo, J.-Y.; Yeh, K.-W.; Chen, T.-K.; Huang, T.-W.; Wu, P.M.; Lee, Y.-C.; Huang, Y.-L.; Chu, Y.-Y.; Yan, D.-C.; et al. Superconductivity in the PbO-type structure α-FeSe. *Proc. Natl. Acad. Sci. USA* **2008**, *105*, 14262–14264. [CrossRef] [PubMed]
4. Nitsche, F.; Goltz, T.; Klauss, H.H.; Isaeva, A.; Müller, U.; Schnelle, W.; Simon, P.; Doert, T.; Ruck, M. Room-Temperature Synthesis, Hydrothermal Recrystallization, and Properties of Metastable Stoichiometric FeSe. *Inorg. Chem.* **2012**, *51*, 7370–7376. [CrossRef] [PubMed]
5. Yoo, H.; Lee, G.-H.; Kim, D.-W. FeSe hollow spheroids as electrocatalysts for high-rate Li–O$_2$ battery cathodes. *J. Alloy. Compd.* **2021**, *856*, 158269. [CrossRef]
6. Li, W.; Niu, Y.; Wu, X.; Wu, F.; Li, T.; Hu, W. Heterostructured CoSe$_2$/FeSe$_2$ Nanoparticles with Abundant Vacancies and Strong Electronic Coupling Supported on Carbon Nanorods for Oxygen Evolution Electrocatalysis. *ACS Sustain. Chem. Eng.* **2020**, *8*, 4658–4666. [CrossRef]
7. Chanda, D.; Tufa, R.A.; Birdja, Y.Y.; Basu, S.; Liu, S. Hydrothermally/electrochemically decorated FeSe on Ni-foam electrode: An efficient bifunctional electrocatalysts for overall water splitting in an alkaline medium. *Int. J. Hydrogen Energy* **2020**, *45*, 27182–27192. [CrossRef]
8. Lv, C.; Liu, H.; Li, D.; Chen, S.; Zhang, H.; She, X.; Guo, X.; Yang, D. Ultrafine FeSe nanoparticles embedded into 3D carbon nanofiber aerogels with FeSe/Carbon interface for efficient and long-life sodium storage. *Carbon* **2019**, *143*, 106–115. [CrossRef]
9. Kwon, J.; Jun, S.W.; Choi, S.I.; Mao, X.; Kim, J.; Koh, E.K.; Kim, Y.-H.; Kim, S.-K.; Hwang, D.Y.; Kim, C.-S.; et al. FeSe quantum dots for in vivo multiphoton biomedical imaging. *Sci. Adv.* **2019**, *5*, eaay0044. [CrossRef]

10. Choi, J.H.; Park, S.-K.; Kang, Y.C. A Salt-Templated Strategy toward Hollow Iron Selenides-Graphitic Carbon Composite Microspheres with Interconnected Multicavities as High-Performance Anode Materials for Sodium-Ion Batteries. *Small* **2019**, *15*, 1803043. [CrossRef]

11. Panda, C.; Menezes, P.W.; Walter, C.; Yao, S.; Miehlich, M.E.; Gutkin, V.; Meyer, K.; Driess, M. From a Molecular 2Fe-2Se Precursor to a Highly Efficient Iron Diselenide Electrocatalyst for Overall Water Splitting. *Angew. Chem. Int. Ed.* **2017**, *56*, 10506–10510. [CrossRef]

12. Qin, Z.; Yang, B.C.; Zhang, S.R.; Li, K.; Yan, S.Q.; Lv, X.W.; Li, Z.J. Flower-like pyrite $FeSe_2$ nanoparticles with enhanced optical properties by hot-injection. *Vacuum* **2015**, *111*, 157–159. [CrossRef]

13. Mao, X.; Kim, J.-G.; Han, J.; Jung, H.S.; Lee, S.G.; Kotov, N.A.; Lee, J. Phase-Pure $FeSe_x$ (x = 1, 2) Nanoparticles with One- and Two-Photon Luminescence. *J. Am. Chem. Soc.* **2014**, *136*, 7189–7192. [CrossRef]

14. Guo, K.; Zou, Z.; Du, J.; Zhao, Y.; Zhou, B.; Xu, C. Coupling $FeSe_2$ with CoSe: An effective strategy to create stable and efficient electrocatalysts for water oxidation. *Chem. Commun.* **2018**, *54*, 11140–11143. [CrossRef]

15. Theerthagiri, J.; Sudha, R.; Premnath, K.; Arunachalam, P.; Madhavan, J.; Al-Mayouf, A.M. Growth of iron diselenide nanorods on graphene oxide nanosheets as advanced electrocatalyst for hydrogen evolution reaction. *Int. J. Hydrogen Energy* **2017**, *42*, 13020–13030. [CrossRef]

16. Gao, R.; Zhang, H.; Yan, D. Iron diselenide nanoplatelets: Stable and efficient water-electrolysis catalysts. *Nano Energy* **2017**, *31*, 90–95. [CrossRef]

17. Xu, X.; Song, F.; Hu, X. A nickel iron diselenide-derived efficient oxygen-evolution catalyst. *Nat. Commun.* **2016**, *7*, 12324. [CrossRef]

18. Yuan, B.; Luan, W.; Tu, S.-t. One-step synthesis of cubic FeS_2 and flower-like $FeSe_2$ particles by a solvothermal reduction process. *Dalton Trans.* **2012**, *41*, 772–776. [CrossRef]

19. Schuster, W.; Mikler, H.; Komarek, K. Transition metal-chalcogen systems, VII.: The iron-selenium phase diagram. *Mon. Für Chem.* **1979**, *110*, 1153–1170. [CrossRef]

20. Terzieff, P.; Komarek, K. The paramagnetic properties of iron selenides with NiAs-type structure. *Mon. Chem.* **1978**, *109*, 651–659. [CrossRef]

21. Hamdadou, N.; Bernède, J.C.; Khelil, A. Preparation of iron selenide films by selenization technique. *J. Cryst. Growth* **2002**, *241*, 313–319. [CrossRef]

22. Feng, Q.J.; Shen, D.Z.; Zhang, J.Y.; Li, B.S.; Li, B.H.; Lu, Y.M.; Fan, X.W.; Liang, H.W. Ferromagnetic FeSe: Structural, electrical, and magnetic properties. *Appl. Phys. Lett.* **2006**, *88*, 012505. [CrossRef]

23. Luo, H.; Furdyna, J.K. The II-VI semiconductor blue-green laser: Challenges and solution. *Semicond. Sci. Technol.* **1995**, *10*, 1041. [CrossRef]

24. Ubale, A.U.; Sakhare, Y.S.; Bhute, M.V.; Belkhedkar, M.R.; Singh, A. Size-dependent structural, electrical and optical properties of nanostructured iron selenide thin films deposited by Chemical Bath Deposition Method. *Solid State Sci.* **2013**, *16*, 134–142. [CrossRef]

25. Ouertani, B.; Ouerfelli, J.; Saadoun, M.; Zribi, M.; Rabha, M.B.; Bessaïs, B.; Ezzaouia, H. Optical and structural properties of $FeSe_2$ thin films obtained by selenization of sprayed amorphous iron oxide films. *Thin Solid Film.* **2006**, *511–512*, 457–462. [CrossRef]

26. Liu, K.W.; Zhang, J.Y.; Shen, D.Z.; Shan, C.X.; Li, B.H.; Lu, Y.M.; Fan, X.W. Electronic and magnetic properties of FeSe thin film prepared on GaAs (001) substrate by metal-organic chemical vapor deposition. *Appl. Phys. Lett.* **2007**, *90*, 262503. [CrossRef]

27. Campos, C.E.M.; de Lima, J.C.; Grandi, T.A.; Machado, K.D.; Drago, V.; Pizani, P.S. XRD, DSC, MS and RS studies of Fe75Se25 iron selenide prepared by mechano-synthesis. *J. Magn. Magn. Mater.* **2004**, *270*, 89–98. [CrossRef]

28. Hamdadou, N.; Khelil, A.; Morsli, M.; Bernàde, J.C. Iron diselenide thin films synthesized by soft selenization of iron films. *Vacuum* **2005**, *77*, 151–156. [CrossRef]

29. Ouertani, B.; Ouerfelli, J.; Saadoun, M.; Bessaïs, B.; Ezzaouia, H.; Bernède, J.C. Transformation of amorphous iron oxide thin films predeposited by spray pyrolysis into a single $FeSe_2$-phase by selenisation. *Sol. Energy Mater. Sol. Cells* **2005**, *87*, 501–511. [CrossRef]

30. Campos, C.E.M.; de Lima, J.C.; Grandi, T.A.; Machado, K.D.; Pizani, P.S. Structural studies of iron selenides prepared by mechanical alloying. *Solid State Commun.* **2002**, *123*, 179–184. [CrossRef]

31. Chang, C.-C.; Wang, C.-H.; Wen, M.-H.; Wu, Y.-R.; Hsieh, Y.-T.; Wu, M.-K. Superconductivity in PbO-type tetragonal FeSe nanoparticles. *Solid State Commun.* **2012**, *152*, 649–652. [CrossRef]

32. Wadia, C.; Alivisatos, A.P.; Kammen, D.M. Materials Availability Expands the Opportunity for Large-Scale Photovoltaics Deployment. *Environ. Sci. Technol.* **2009**, *43*, 2072–2077. [CrossRef]

33. Luther, G.W. Pyrite synthesis via polysulfide compounds. *Geochim. Cosmochim. Acta* **1991**, *55*, 2839–2849. [CrossRef]

34. Ennaoui, A.; Fiechter, S.; Pettenkofer, C.; Alonso-Vante, N.; Büker, K.; Bronold, M.; Höpfner, C.; Tributsch, H. Iron disulfide for solar energy conversion. *Sol. Energy Mater. Sol. Cells* **1993**, *29*, 289–370. [CrossRef]

35. Kwon, H.; Thanikaikarasan, S.; Mahalingam, T.; Park, K.; Sanjeeviraja, C.; Kim, Y. Characterization of electrosynthesized iron diselenide thin films. *J. Mater. Sci. Mater. Electron.* **2008**, *19*, 1086–1091. [CrossRef]

36. Akhtar, M.; Akhtar, J.; Malik, M.A.; Tuna, F.; Helliwell, M.; O'Brien, P. Deposition of iron selenide nanocrystals and thin films from *tris*(*N*,*N*-diethyl-*N*′-naphthoylselenoureato)iron(iii). *J. Mater. Chem.* **2012**, *22*, 14970–14975. [CrossRef]

37. Shi, W.; Zhang, X.; Che, G.; Fan, W.; Liu, C. Controlled hydrothermal synthesis and magnetic properties of three-dimensional FeSe$_2$ rod clusters and microspheres. *Chem. Eng. J.* **2013**, *215–216*, 508–516. [CrossRef]

38. Sines, I.T.; Schaak, R.E. Phase-Selective Chemical Extraction of Selenium and Sulfur from Nanoscale Metal Chalcogenides: A General Strategy for Synthesis, Purification, and Phase Targeting. *J. Am. Chem. Soc.* **2010**, *133*, 1294–1297. [CrossRef]

39. Chen, L.; Yang, X.; Fu, X.; Wang, C.; Liang, C.; Wu, M. Facile Solvothermal Synthesis of Uniform Iron Selenide Nanoplates. *Eur. J. Inorg. Chem.* **2011**, *2011*, 2098–2102. [CrossRef]

40. Owen, J.; Brus, L. Chemical Synthesis and Luminescence Applications of Colloidal Semiconductor Quantum Dots. *J. Am. Chem. Soc.* **2017**, *139*, 10939–10943. [CrossRef]

41. García-Rodríguez, R.; Hendricks, M.P.; Cossairt, B.M.; Liu, H.; Owen, J.S. Conversion Reactions of Cadmium Chalcogenide Nanocrystal Precursors. *Chem. Mater.* **2013**, *25*, 1233–1249. [CrossRef]

42. Sowers, K.L.; Swartz, B.; Krauss, T.D. Chemical Mechanisms of Semiconductor Nanocrystal Synthesis. *Chem. Mater.* **2013**, *25*, 1351–1362. [CrossRef]

43. Benito-Alifonso, D.; Tremel, S.; Hou, B.; Lockyear, H.; Mantell, J.; Fermín, D.J.; Verkade, P.; Berry, M.; Galan, M.C. Lactose as a "Trojan horse" for Quantum Dot Cell Transport. *Angew. Chem. Int. Ed.* **2013**, *53*, 810–814. [CrossRef]

44. Hou, B. Colloidal Quantum Dots: The Artificial Building Blocks for New-Generation Photo-Electronics and Photochemistry. *Isr. J. Chem.* **2019**, *59*, 637–638. [CrossRef]

45. Hou, B.; Benito-Alifonso, D.; Webster, R.; Cherns, D.; Galan, M.C.; Fermín, D.J. Rapid phosphine-free synthesis of CdSe quantum dots: Promoting the generation of Se precursors using a radical initiator. *J. Mater. Chem. A* **2014**, *2*, 6879–6886. [CrossRef]

46. Hou, B.; Parker, D.; Kissling, G.P.; Jones, J.A.; Cherns, D.; Fermín, D.J. Structure and Band Edge Energy of Highly Luminescent CdSe$_{1-x}$Te$_x$ Alloyed Quantum Dots. *J. Phys. Chem. C* **2013**, *117*, 6814–6820. [CrossRef]

47. Sayevich, V.; Robinson, Z.L.; Kim, Y.; Kozlov, O.V.; Jung, H.; Nakotte, T.; Park, Y.-S.; Klimov, V.I. Highly versatile near-infrared emitters based on an atomically defined HgS interlayer embedded into a CdSe/CdS quantum dot. *Nat. Nanotechnol.* **2021**. [CrossRef]

48. Dai, X.; Zhang, Z.; Jin, Y.; Niu, Y.; Cao, H.; Liang, X.; Chen, L.; Wang, J.; Peng, X. Solution-processed, high-performance light-emitting diodes based on quantum dots. *Nature* **2014**, *515*, 96–99. [CrossRef]

49. Shen, H.; Gao, Q.; Zhang, Y.; Lin, Y.; Lin, Q.; Li, Z.; Chen, L.; Zeng, Z.; Li, X.; Jia, Y.; et al. Visible quantum dot light-emitting diodes with simultaneous high brightness and efficiency. *Nat. Photonics* **2019**, *13*, 192–197. [CrossRef]

50. Zhao, Q.; Gouget, G.; Guo, J.; Yang, S.; Zhao, T.; Straus, D.B.; Qian, C.; Oh, N.; Wang, H.; Murray, C.B.; et al. Enhanced Carrier Transport in Strongly Coupled, Epitaxially Fused CdSe Nanocrystal Solids. *Nano Lett.* **2021**, *21*, 3318–3324. [CrossRef]

51. Banski, M.; Afzaal, M.; Malik, M.A.; Podhorodecki, A.; Misiewicz, J.; O'Brien, P. Special Role for Zinc Stearate and Octadecene in the Synthesis of Luminescent ZnSe Nanocrystals. *Chem. Mater.* **2015**, *27*, 3797–3800. [CrossRef]

52. Hou, B.; Li, Y.; Liu, Y.; Yuan, B.; Jia, M.; Jiang, F. A simple way of shape-controlled synthesis of ZnSe nanocrystals: Nanodots, nanoflowers, and nanotubes. *CrystEngComm* **2009**, *11*, 1789–1792. [CrossRef]

53. Kim, T.; Kim, K.-H.; Kim, S.; Choi, S.-M.; Jang, H.; Seo, H.-K.; Lee, H.; Chung, D.-Y.; Jang, E. Efficient and stable blue quantum dot light-emitting diode. *Nature* **2020**, *586*, 385–389. [CrossRef] [PubMed]

54. Han, C.-Y.; Lee, S.-H.; Song, S.-W.; Yoon, S.-Y.; Jo, J.-H.; Jo, D.-Y.; Kim, H.-M.; Lee, B.-J.; Kim, H.-S.; Yang, H. More Than 9% Efficient ZnSeTe Quantum Dot-Based Blue Electroluminescent Devices. *ACS Energy Lett.* **2020**, *5*, 1568–1576. [CrossRef]

55. Hou, B.; Sohn, M.; Lee, Y.-W.; Zhang, J.; Sohn, J.I.; Kim, H.; Cha, S.; Kim, J.M. Chemically encoded self-organized quantum chain supracrystals with exceptional charge and ion transport properties. *Nano Energy* **2019**, *62*, 764–771. [CrossRef]

56. Song, H.; Lin, Y.; Zhang, Z.; Rao, H.; Wang, W.; Fang, Y.; Pan, Z.; Zhong, X. Improving the Efficiency of Quantum Dot Sensitized Solar Cells beyond 15% via Secondary Deposition. *J. Am. Chem. Soc.* **2021**, *143*, 4790–4800. [CrossRef] [PubMed]

57. Song, H.; Lin, Y.; Zhou, M.; Rao, H.; Pan, Z.; Zhong, X. Zn-Cu-In-S-Se Quinary "Green" Alloyed Quantum-Dot-Sensitized Solar Cells with a Certified Efficiency of 14.4%. *Angew. Chem. Int. Ed.* **2021**, *60*, 6137–6144. [CrossRef]

58. Kattan, N.; Hou, B.; Fermín, D.J.; Cherns, D. Crystal structure and defects visualization of Cu$_2$ZnSnS$_4$ nanoparticles employing transmission electron microscopy and electron diffraction. *Appl. Mater. Today* **2015**, *1*, 52–59. [CrossRef]

59. Hou, B.; Benito-Alifonso, D.; Kattan, N.; Cherns, D.; Galan, M.C.; Fermín, D.J. Initial Stages in the Formation of Cu$_2$ZnSn(S,Se)$_4$ Nanoparticles. *Chem. A Eur. J.* **2013**, *19*, 15847–15851. [CrossRef]

60. Hou, B.; Cho, Y.; Kim, B.S.; Hong, J.; Park, J.B.; Ahn, S.J.; Sohn, J.I.; Cha, S.; Kim, J.M. Highly Monodispersed PbS Quantum Dots for Outstanding Cascaded-Junction Solar Cells. *ACS Energy Lett.* **2016**, *1*, 834–839. [CrossRef]

61. Hou, B.; Cho, Y.; Kim, B.-S.; Ahn, D.; Lee, S.; Park, J.B.; Lee, Y.-W.; Hong, J.; Im, H.; Morris, S.M.; et al. Red green blue emissive lead sulfide quantum dots: Heterogeneous synthesis and applications. *J. Mater. Chem. C* **2017**, *5*, 3692–3698. [CrossRef]

62. Hou, B.; Kim, B.-S.; Lee, H.K.H.; Cho, Y.; Giraud, P.; Liu, M.; Zhang, J.; Davies, M.L.; Durrant, J.R.; Tsoi, W.C.; et al. Multi-photon Absorption Stimulated Metal Chalcogenide Quantum Dot Solar Cells under Ambient and Concentrated Irradiance. *Adv. Funct. Mater.* **2020**, *30*, 2004563. [CrossRef]

63. Hou, B.; Jung, S.-H.; Zhang, J.; Hong, Y.; Kim, B.-S.; Sohn, J.I.; Lee, E.K.; Choi, B.L.; Whang, D.; Cha, S.; et al. Growth of quantum dot coated core-shell anisotropic nanowires for improved thermal and electronic transport. *Appl. Phys. Lett.* **2019**, *114*, 243104. [CrossRef]

64. Campos, M.P.; Hendricks, M.P.; Beecher, A.N.; Walravens, W.; Swain, R.A.; Cleveland, G.T.; Hens, Z.; Sfeir, M.Y.; Owen, J.S. A Library of Selenourea Precursors to PbSe Nanocrystals with Size Distributions near the Homogeneous Limit. *J. Am. Chem. Soc.* **2017**, *139*, 2296–2305. [CrossRef]
65. Shrestha, A.; Batmunkh, M.; Tricoli, A.; Qiao, S.Z.; Dai, S. Near-Infrared Active Lead Chalcogenide Quantum Dots: Preparation, Post-Synthesis Ligand Exchange, and Applications in Solar Cells. *Angew. Chem. Int. Ed.* **2019**, *58*, 5202–5224. [CrossRef]
66. Lin, Q.; Yun, H.J.; Liu, W.; Song, H.-J.; Makarov, N.S.; Isaienko, O.; Nakotte, T.; Chen, G.; Luo, H.; Klimov, V.I.; et al. Phase-Transfer Ligand Exchange of Lead Chalcogenide Quantum Dots for Direct Deposition of Thick, Highly Conductive Films. *J. Am. Chem. Soc.* **2017**, *139*, 6644–6653. [CrossRef]
67. Livache, C.; Martinez, B.; Goubet, N.; Gréboval, C.; Qu, J.; Chu, A.; Royer, S.; Ithurria, S.; Silly, M.G.; Dubertret, B.; et al. A colloidal quantum dot infrared photodetector and its use for intraband detection. *Nat. Commun.* **2019**, *10*, 2125. [CrossRef]
68. Tang, X.; Wu, G.f.; Lai, K.W.C. Plasmon resonance enhanced colloidal HgSe quantum dot filterless narrowband photodetectors for mid-wave infrared. *J. Mater. Chem. C* **2017**, *5*, 362–369. [CrossRef]
69. Qu, J.; Rastogi, P.; Gréboval, C.; Lagarde, D.; Chu, A.; Dabard, C.; Khalili, A.; Cruguel, H.; Robert, C.; Xu, X.Z.; et al. Electroluminescence from HgTe Nanocrystals and Its Use for Active Imaging. *Nano Lett.* **2020**, *20*, 6185–6190. [CrossRef]
70. Ma, Y.; Zhang, Y.; Yu, W.W. Near infrared emitting quantum dots: Synthesis, luminescence properties and applications. *J. Mater. Chem. C* **2019**, *7*, 13662–13679. [CrossRef]
71. Yarema, M.; Yarema, O.; Lin, W.M.M.; Volk, S.; Yazdani, N.; Bozyigit, D.; Wood, V. Upscaling Colloidal Nanocrystal Hot-Injection Syntheses via Reactor Underpressure. *Chem. Mater.* **2017**, *29*, 796–803. [CrossRef]
72. Li, D.; Pan, D.; Liu, W.; Li, X.; Chen, M.; Li, S.; Li, Y.; Tan, J.; Sun, D.; Wang, Z.; et al. Controllable Phase Transition for Layered β-FeSe Superconductor Synthesized by Solution Chemistry. *Chem. Mater.* **2017**, *29*, 842–848. [CrossRef]
73. Greenfield, J.T.; Kamali, S.; Lee, K.; Kovnir, K. A Solution for Solution-Produced β-FeSe: Elucidating and Overcoming Factors that Prevent Superconductivity. *Chem. Mater.* **2015**, *27*, 588–596. [CrossRef]
74. Oyler, K.D.; Ke, X.; Sines, I.T.; Schiffer, P.; Schaak, R.E. Chemical Synthesis of Two-Dimensional Iron Chalcogenide Nanosheets: FeSe, FeTe, Fe(Se,Te), and FeTe$_2$. *Chem. Mater.* **2009**, *21*, 3655–3661. [CrossRef]
75. Liu, H.; Owen, J.S.; Alivisatos, A.P. Mechanistic Study of Precursor Evolution in Colloidal Group II−VI Semiconductor Nanocrystal Synthesis. *J. Am. Chem. Soc.* **2006**, *129*, 305–312. [CrossRef]
76. Tauc, J. Optical properties and electronic structure of amorphous Ge and Si. *Mater. Res. Bull.* **1968**, *3*, 37–46. [CrossRef]
77. Bass, M.; DeCusatis, C.; Enoch, J.; Lakshminarayanan, V.; Li, G.; MacDonald, C.; Maha- jan, V.; Van Stryland, E. Optical Properties of Materials, Nonlinear Optics, Quantum Optics. In *Handbook of Optics*, 3rd ed.; Mcgraw-Hill: New York, NY, USA, 2009; Volume IV.
78. Bass, M. *Handbook of Optics*, 2nd ed.; Mcgraw-Hill: New York, NY, USA, 1994; Volume II.
79. Devore, J.R. Refractive Indices of Rutile and Sphalerite. *J. Opt. Soc. Am.* **1951**, *41*, 416–417. [CrossRef]